

# Detached Eddy Simulation of Flap Side-Edge Flow

Shankar Kumar Balakrishnan\* and Karim Shariff†

*NASA Ames Research Center, Moffett Field, California 94035, USA*

Detached Eddy Simulation (DES) of flap side-edge flow is performed with a NACA 63<sub>2</sub>-215 wing and 30% chord, half-span flap configuration at a wing chord based Reynolds number of 3.7 million. This configuration has been used in previous experimental studies<sup>1,2</sup> and Reynolds Averaged Navier-Stokes (RANS) simulations<sup>3,4</sup> to understand the aerodynamic characteristics of the mean flap side-edge flow field. Aeroacoustic measurements<sup>5,6</sup> have also been obtained for this configuration at a wing-chord Reynolds number of 1.7 million. In the present study, a RANS simulation is first performed as a precursor to the DES and the results are shown to closely match the experiments and the previous RANS study.<sup>3</sup> The key unsteady features of the statistically stationary flap side-edge flowfield from the DES are presented. An instability of the rolled-up vortex near the leading edge of the flap side is identified to lead to the breakdown to turbulence of the side-edge flow field and is a potential key contributor to far-field noise.

## Nomenclature

$Re$	Reynolds number based on main wing chord
$x$	Streamwise direction
$y$	Vertical direction
$z$	Spanwise direction
$\mathbf{u}$	Velocity vector
$\boldsymbol{\omega}$	Vorticity vector
$U_\infty$	Freestream velocity
$c$	Main wing chord
$c_f$	Flap chord
$x_f$	Location along flap chord
$C_p$	Surface pressure coefficient
$\hat{\mathbf{t}}$	Unit side-edge tangent vector
$\hat{\mathbf{n}}$	Unit outward surface normal vector
$\hat{\mathbf{k}}$	Unit vector along positive spanwise direction
$\hat{p}$	Temporal Fourier coefficient of pressure field

## I. Introduction

Increasingly stringent noise regulations at airports have driven research efforts to identify the various sources of aircraft noise and develop suitable noise reduction strategies. With the reduction in engine noise due to the adoption of high-bypass ratio engines, airframe noise now forms a significant part of overall aircraft noise<sup>7</sup> and is nearly equal to the engine noise in the approach configuration. Reducing airframe noise is therefore essential for further reductions in aircraft noise. Flap side-edge noise has been identified as a dominant source of airframe noise<sup>8,9</sup> due to the presence of an unsteady vortical flow field that acts as a noise source in the vicinity of the flap side-edge, which can efficiently scatter the noise to the far field.

---

\*NASA Postdoctoral Program Fellow, Computational Aerosciences branch, Mail Stop 258-5.

†Research Scientist, Computational Aerosciences branch

A good understanding of the unsteady flap side-edge flow field is required in order to develop accurate noise prediction methods and appropriate noise mitigation strategies. Experiments and RANS simulations<sup>1–3</sup> revealed the following features of the mean flow field (see figure 5) : Flow separates at the side-edges of the pressure and suction sides of the flap side-edge and the shear layers roll up to form a primary and secondary vortex respectively. The vortices grow in size along the streamwise direction until the primary vortex crosses over to the suction side and undergoes a merger with the secondary vortex. The merged vortex is located above the suction side and is fed continually by the curved shear layers shed at the side edges of the flap. Under certain conditions, this merged vortex undergoes a vortex breakdown above the trailing edge of the flap due to the presence of an adverse pressure gradient. Aeroacoustic measurements<sup>5,6</sup> were also performed for this wing and half-span flap configuration which showed that the centroid of the noise source map at high frequencies was located closer to the leading edge. With decreasing frequency, the centroid moved downstream.

Various analytical models of flap side-edge noise have been proposed. The earliest models proposed by Hardin<sup>10</sup> and Meecham<sup>11</sup> considered two-dimensional flow with a point streamwise vortex representing boundary-layer turbulence being accelerated around an edge by the spanwise flow. Howe<sup>12</sup> considered the effect of the presence of the main wing adjacent to the side-edge of a deflected flap. Sen<sup>13</sup> modeled the production of noise due to the oscillation of vortex position about a point of stable equilibrium. His vortex corresponds to the merged vortex described in the experimental and numerical studies of flap side-edge flow. The source of the oscillations in Sen’s model is a large-scale flow structure in the edge-vorticity distribution near the pressure side edge.

Khorrami and Singer<sup>14</sup> identified large-scale fluctuations of the curved free shear layer emanating from the pressure side-edge and of the postmerged vortex located above the suction side-edge, downstream of the midchord region as the potential principal noise sources in addition to the turbulent boundary layer convecting past the side-edges, the vortex merger and the vortex breakdown as the other sources. They used the time-averaged flow field obtained from previous experiments<sup>2</sup> and computations<sup>3</sup> to perform a linear temporal stability analysis of the merged vortex and the curved shear layer. For a flap deflection of 29°, the postmerged vortex attains an axisymmetric state with a jet-like axial velocity distribution. For this case, they fitted the profile of the similarity solution obtained by Batchelor<sup>15</sup> to the merged vortex and the profile from Michalke and Timme<sup>16</sup> to the curved shear layer. The frequency range of the unstable modes was found to be within the range of the unsteady surface pressure spectra in the aeroacoustic measurements.<sup>5</sup>

Imamura et al.<sup>17</sup> performed DES and LES of flow around a NACA0012 wingtip and showed that the aerodynamics at the wingtip was similar to that at a flap side-edge. They found that the core of the primary vortex (using the terminology in this paper, see figure 5) was unsteady and that the secondary vortex core was relatively more steady before the vortex merger occurred. The unsteady surface pressure distribution on the wing surface showed that the presence of a broadband noise source along the side face of the wing and a low frequency source over the suction surface. These results were consistent with the key noise sources – the instability of the shear layer and that of the merged vortex, that had been identified in previous work.<sup>14,18</sup> Langtry et al.<sup>19</sup> performed a DES of the flap side-edge flow using a sub-domain approach. The steady RANS solution for flow over the entire wing geometry was used to provide the boundary conditions for a DES performed within a smaller domain enclosing the flap side-edge. They captured the break up to turbulence of the side-edge vortices.

The present DES aims to provide a more complete picture of the unsteady flap side-edge flow field that would help determine the noise sources. The underlying instabilities giving rise to the unsteadiness are suggested.

## II. Configuration

The configuration used in this study consists of a main wing having a NACA 63<sub>2</sub>–215 Mod B section and a 30% chord, half-span slotted flap (Figure 1). The flapped half-span of the wing includes a trailing edge cove. In figure 1, the spanwise ends of the geometry are attached to side-walls. The region of interest is the flap side located at the midspan ( $z = 0$ ) plane. A model with this configuration and a main wing chord (with flap stowed) of 2.5 feet and a span of 5 feet was used in the experimental study carried out in the 7 by 10 ft. wind tunnel at the NASA Ames Research Center.<sup>1</sup> The experiment was performed at a wing chord based Reynolds number of 3.7 million and a free stream Mach number of 0.22. The angle-of-attack of the main wing was 10 deg. and two flap deflections of 29 deg. and 39 deg. were tested. These values were

chosen to represent an aircraft landing configuration. In the present study the 39 deg. flap deflection setting from this experiment was chosen to be simulated.

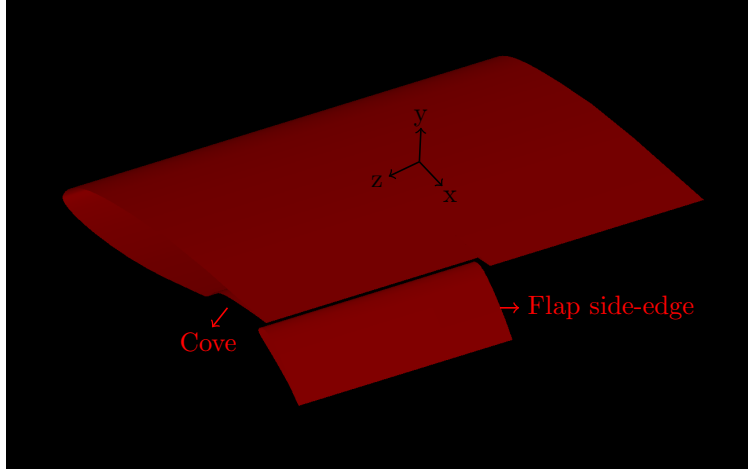


Figure 1. Simulated wing and half-span flap configuration with a flap deflection of 39 deg.

A companion experiment using a smaller size model was performed at the NASA Langley Quiet Flow Facility.<sup>2</sup> Since this experiment was performed in an open-jet facility, while the same flap deflections were used as in the Ames experiment, the angle-of-attack of the main wing and the gap and overlap between the wing and flap were varied in order to produce a similar surface pressure distribution. Flow speeds of up to Mach number of 0.17 were tested resulting in wing-chord based Reynolds number up to 1.7 million.

Khorrami et al<sup>3</sup> performed a thin-layer compressible RANS simulation of the Ames experiment using the Spalart-Allmaras turbulence model. They obtained a surface pressure distribution which matched both the experiments closely and captured the key features of the flap side-edge flow field including the vortex breakdown at the higher flap deflection setting.

Aeroacoustic measurements were performed at the Langley Quiet Flow Facility<sup>5,6</sup> using the same configuration and flow conditions as in Ref. 2. Unsteady surface pressure measurements were obtained at various locations on the flap side and on the pressure and suction sides near the edges.

### III. Flow solver and turbulence model

The unstructured finite-volume based, incompressible Navier-Stokes solver CDP v2.3, developed at Stanford University's Center for Integrated Turbulence Simulations (CITS), was used for the numerical simulations. The code employs a collocated formulation which conserves kinetic energy in the inviscid limit. The spatial discretization is second-order accurate and the time advancement is performed using a second-order implicit fractional step method. The details of the numerical scheme are provided in Ham and Iaccarino<sup>20</sup> and Mahesh et al.<sup>21</sup>

RANS simulations were performed using the Spalart-Allmaras turbulence model. Second-order central differencing was used for the viscous terms in the momentum and scalar (turbulent viscosity) equations and a first-order upwinding scheme was used for the convection term in the scalar equation. First-order upwinding treatment was used for the convection terms in the momentum equation.

The DES simulation was performed using the Spalart-Allmaras based delayed-DES (DDES) model.<sup>22</sup> The largest cell dimension was chosen as the LES filter width. The calibrated value of  $C_{DES}$  for homogeneous turbulence<sup>23</sup> of 0.65 was used. In the DES, a weighted combination of central differencing and upwind differencing with 10% upwinding was used for the convective terms of the momentum equation. The treatment of the other terms was the same as in the RANS.

## IV. Computational grid and domain

The dimensions of the computational domain and the location of the geometry within the domain were the same as in the previous RANS study of Khorrami et al.<sup>3</sup> which simulated the NASA Ames experiment including the wind tunnel walls. Uniform inflow and extrapolation outflow conditions were applied 15 main wing chord lengths upstream and downstream of the wing leading edge, respectively. The height and width of the test section were 4 and 2.25 chord lengths respectively. The wind tunnel walls were treated as free-slip boundaries and the wing and flap surfaces as no-slip boundaries. The wing span of  $2.25c$  differs from the value of  $2.0c$  in the experiment. Khorrami et al. chose this value for historical reasons. However it is seen in both the experiment and their RANS study that the spanwise variation in the flow ceases well away from the side walls. Hence this difference is not expected to affect the comparison with the experiment as long as the flow quantities located at the same distance from the mid-span are considered.

The grid was first generated on a cross-section (with its normal along the spanwise direction) of the domain at a spanwise location where the flap is present and on the side-face of the flap (see figure 2). The grid on these cross-sections were largely composed of quadrilateral elements with some triangular elements used in near the leading and trailing ends of the flap side-face and the cove side-face. The grid on the regions excluding the flap side-face and the cove side-face were extruded along the entire wing span. The grid on the flap and cove side-faces were extruded from  $z = 0$  to  $z = -1.125c$  and from  $z = 0$  to  $z = 1.125c$  respectively. The resulting three-dimensional grid has hexahedral and triangular prism elements.

For both the precursor RANS and the DES, a grid with 98.2 million cells was used. The typical wall normal spacing around the flap leading-edge is  $5 \times 10^{-6}c$ . This resulted in a  $y^+$  value for the first cell off the wall of approximately 1. Figure 3 highlights the resolution in the flap side-edge region using a cross-section of the grid normal to the streamwise direction at a streamwise location containing the flap. The resolution in this region was chosen to be fine enough to capture the small-scale structures generated during the unsteady simulation.

## V. Results

### V.A. Precursor RANS

Convergence of the RANS solution to a steady state was tracked using the lift, drag, and pitching moment values for the combined wing-flap model. A converged RANS solution was obtained after  $\approx 7.50$  main chord flow-through times. The surface pressure coefficient ( $C_p$ ) distribution at different spanwise locations ( $z = 0$  is the midspan location) from the converged solution are presented in figure 4 along with the distributions from the experiment and the previous RANS study. The spanwise locations from the previous RANS are as reported in Khorrami et al.<sup>3</sup> Since the present computation is incompressible while the free-stream Mach number is  $M_\infty = 0.2$ , the Karman-Tsien compressibility correction has been applied to the  $C_p$  values from the present RANS. The  $C_p$  distribution is seen to match the experiment and the previous RANS closely with only minor differences. The kink in the  $-C_p$  distribution on the lower surface of the main wing near  $x/c \approx 0.7$  (on the half-span side with the cove) corresponds to the leading edge of the cove. On the main wing, the  $C_p$  distribution from the present RANS follows the distribution from the experiment more closely than the previous RANS, especially in the region aft of the cove leading edge. On the flap however, both RANS simulations match each other closely but overpredict the value of  $-C_p$  as compared to the experiment.

The key features of the time-averaged flap side-edge flow field — the roll-up of the primary and secondary vortices, their growth along the flap chord, the cross-over of the primary vortex to the suction side and the vortex merger are captured (Figure 5). A comparison of contours of streamwise vorticity at three locations along the flap chord between the experiment and both the RANS studies is provided in Figure 6. At the first two stations, the vortex structures from the RANS results are in agreement with each other but are more diffused in comparison with the experiment.

### V.B. DES

The converged RANS solution was used as the initial condition for the DES. The statistical stationarity of the DES solution was verified by tracking the instantaneous pressure and velocity magnitude at probes located around the flap side-edge. The probes were located along the path of the primary vortex and at the location where the vortex merger occurs.



(a) At a spanwise location containing the flap



(b) At the mid-span showing the grid on the flap side-face

**Figure 2. Cross-sections of the grid with their normal along spanwise ( $z$ ) direction.**

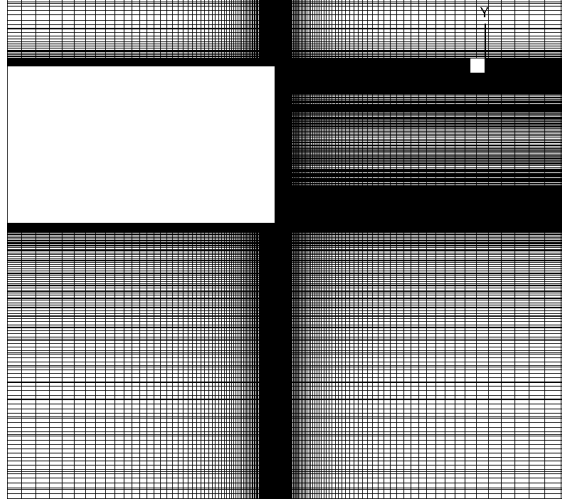


Figure 3. A cross-section of the grid with its normal along the streamwise ( $x$ ) direction highlighting the resolution in the flap side-edge region.

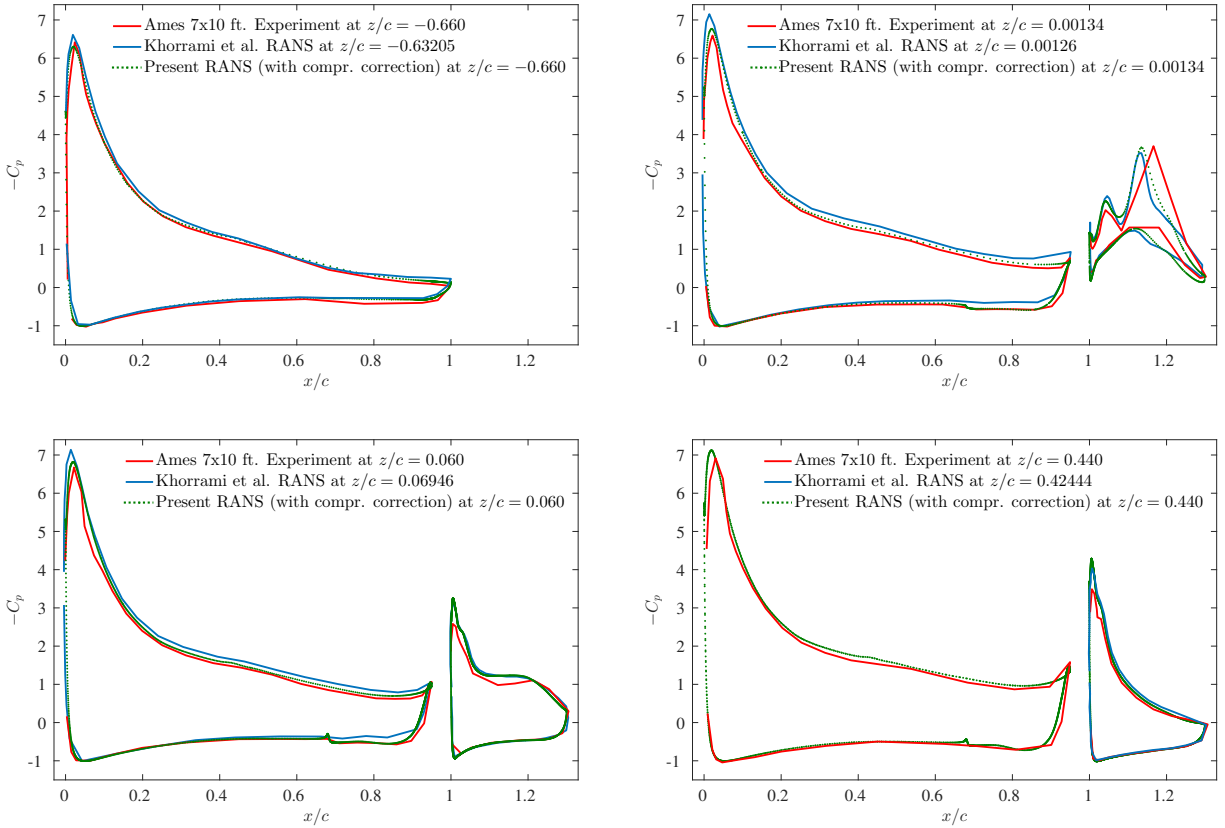
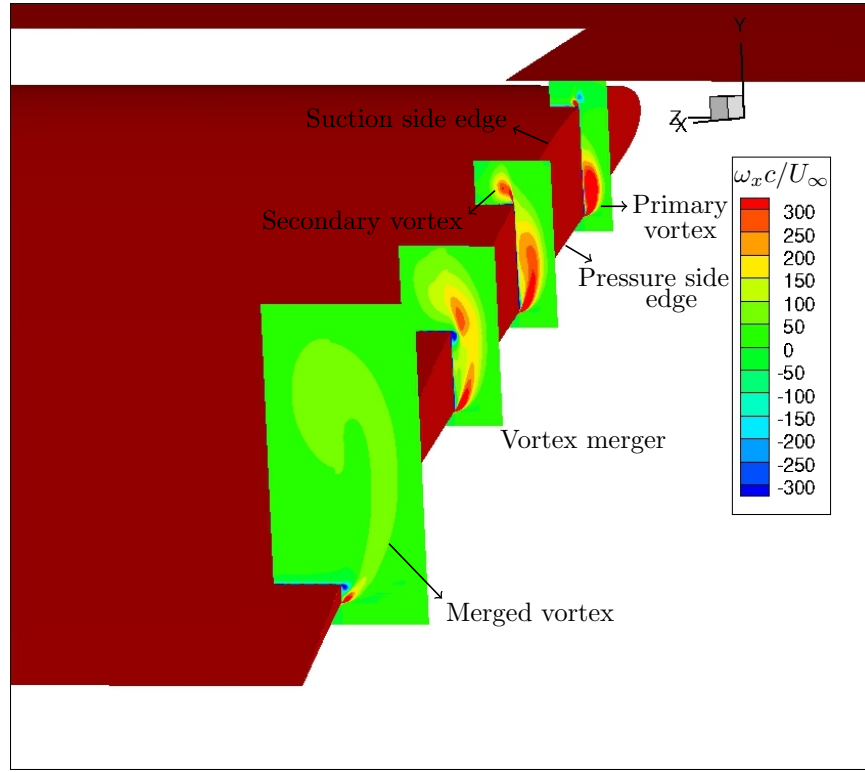


Figure 4. Comparison of the surface pressure coefficient distributions at different spanwise locations. Positive values of  $z/c$  correspond to the half-span which includes the flap. The  $x$ -axis values are the locations along the main wing and flap chords. The flap leading edge is arbitrarily chosen to be at  $x/c = 1.0$ . The  $-C_p$  distribution on the main wing at  $z/c = 0.440$  is not available from Khorrami et al.<sup>3</sup>



**Figure 5.** Normalized streamwise vorticity ( $\omega_x c / U_\infty$ ) at different chordwise locations along the flap from the steady RANS solution.

A temporal mean of the flowfield was computed from samples obtained with time spacing of  $\Delta t = 0.0015c/U_\infty$  from a time period of  $0.186c/U_\infty$ . Contours of streamwise vorticity in planes normal to the flap chord from the DES mean flowfield are compared with the experiment and the RANS studies in Figure 6. At the first chordwise station, it is observed that compared to the experiment, both RANS calculations predict a larger primary vortex. The DES mean gives a good prediction of the size of the primary vortex and also captures the feeding sheet for this vortex with a ‘hill-like’ feature of negative streamwise vorticity (blue) beneath it. The vortex structures seen at the top of the DES mean plot are from a vortex sheet shed by the main wing. At the second chordwise location, the dual vortex structure above the suction surface of the flap is captured in the RANS as well as in the DES mean. At this station also the feeding sheet is less diffuse compared to the RANS solutions. At the third chordwise location, the height of the merged vortex above the flap surface is slightly higher than in the experiment.

Figure 7 presents an isosurface of instantaneous vorticity magnitude colored by the helicity field. The rolled-up primary vortex is seen to be turbulent along the entire flap side face. The contours of helicity indicate that the vortices have significant axial flow. The lower level vorticity magnitude isosurface in figure 8 shows that the secondary vortex is relatively more steady. This behaviour is similar to that observed by Imamura et al.<sup>17</sup> for wingtip flow. The instability of the vortex sheet shed from the trailing edge of the main wing is also highlighted in this figure. The vortex sheets shed from the trailing edge of the main wing (vorticity along spanwise direction) and from the side edge of the main wing at the mid-span location (vorticity along streamwise direction) both roll up to form vortices. The contour map of the spanwise vorticity on the midspan plane (Figure 9) shows the unsteady merged vortex located above the flap. Instantaneous streamlines coloured by the streamwise velocity are presented in figure 10. The region of negative streamwise velocity within the core of the merged vortex corresponds to the recirculation region created by the vortex breakdown.



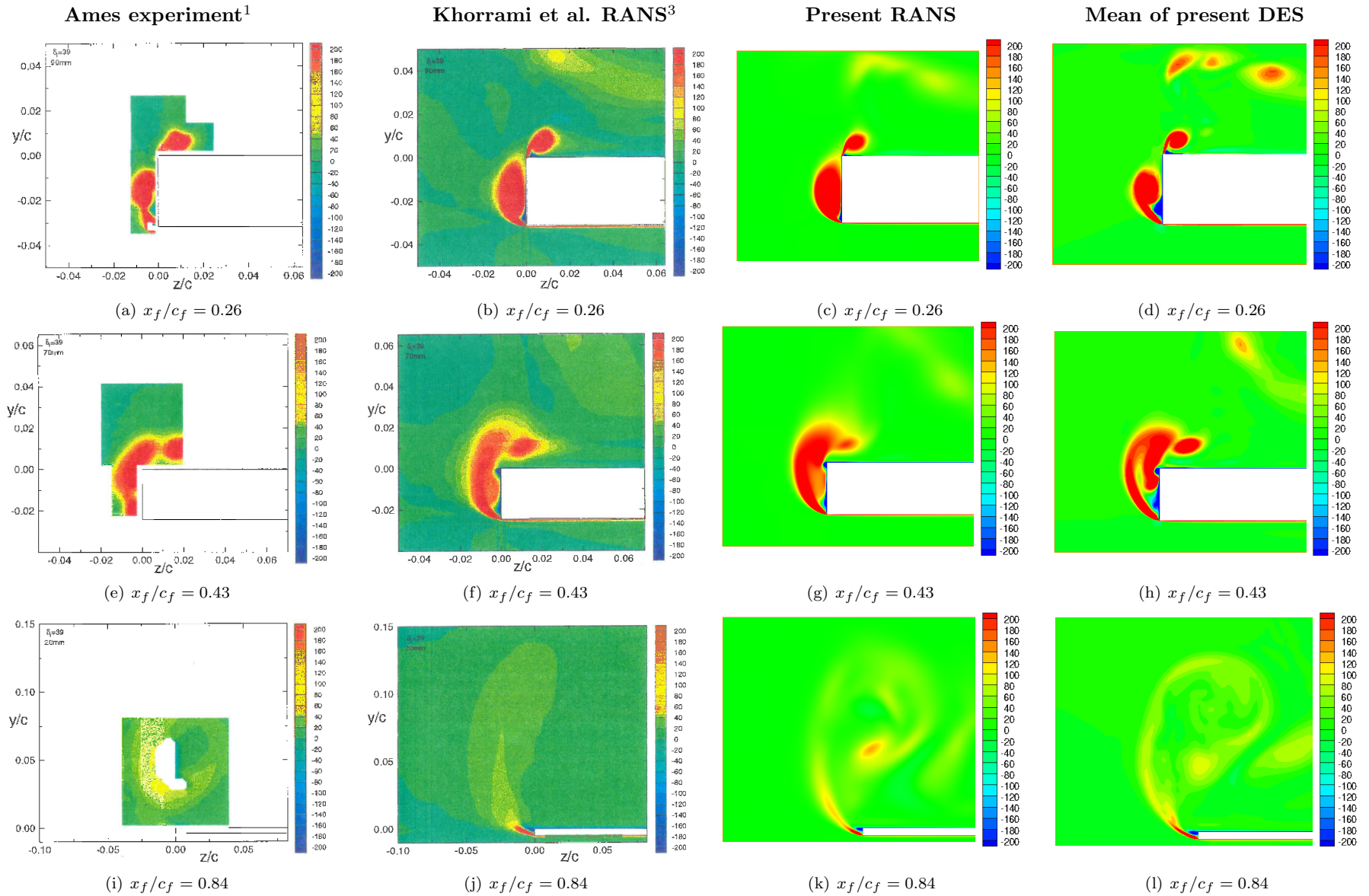


Figure 6. Contours of streamwise vorticity ( $\omega_x c/U_\infty$ ) on planes normal to the flap chord at different chordwise locations from the NASA Ames experiment,<sup>1</sup> the previous RANS by Khorrami et al.<sup>3</sup> for the 39 deg. case, the present RANS and the mean flowfield from the DES. The view is from an upstream location looking along the downstream direction.



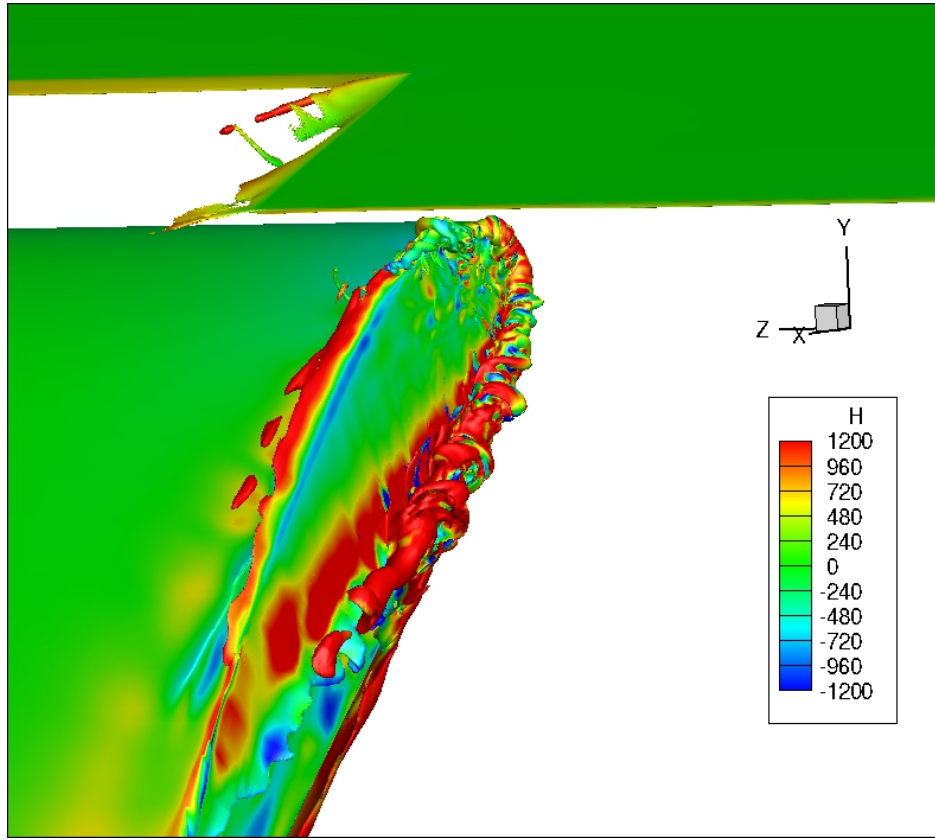


Figure 7. Isosurface of instantaneous vorticity magnitude,  $|\omega| = 1000 U_\infty/c$  colored by the normalized helicity  $H = (\mathbf{u} \cdot \boldsymbol{\omega})c/U_\infty^2$  from the DES.

#### V.B.1. Leading edge instability of primary vortex

An alternate DES simulation was performed using twice the LES filter width as defined in section III. By filtering out the small scale structures the basic structure of the instability leading to the breakdown to turbulence was highlighted. Isosurfaces of vorticity (Figure 11a) from this large-filter DES shows the helical structure of the instability of the rolled-up vortex near the leading edge of the flap. The contour map of vorticity magnitude on a slice through the vortex (Figure 11b) suggests that the helical instability has a shape associated with an  $m = 2$  azimuthal mode.

A description of the kinematics of the flap side-edge flowfield is now provided in order to understand the location of the instability. Consider the unit vector  $\hat{t}$  which is tangent to the flap side-edge contour and directed such that  $\hat{t} \times \hat{n} = \hat{k}$  where  $\hat{n}$  is the unit outward normal to the side-edge contour and  $\hat{k}$  is the unit vector along the  $z$ -direction (see figure 12). At each location on the flap side-edge, flow separation occurs in two different ways: (Type 1) The boundary layer on either the suction side or the pressure side of the flap rolls up to form a vortex with the vorticity directed predominantly along the local  $-\hat{t}$  direction (Type 2) The boundary layer on the side-face of the flap rolls up to a vortex with the vorticity directed predominantly along the local  $\hat{t}$  direction. Figure 12 illustrates this description using an isosurface of vorticity magnitude colored by the component of vorticity along the local side-edge tangent vector from the steady RANS solution. It can be seen that the flow separation from the side-edge switches from type (1) to type (2) at a location near the leading edge on the suction side of the flap. The primary and secondary vortices described in the literature are those formed respectively due to flow separation of type (1) and (2). Although the primary vortex is predominantly located on the pressure side of the flap, it begins from this switching location on the suction side.

It can be seen now that the instability in figure 7 occurs in the primary vortex near the leading edge location at which the primary vortex begins. The helical structure of the instability suggests the possibility that it is an instance of the well-known family of instabilities occurring in columnar vortices with axial flow. The stability of vortices with axial flow has been studied extensively for decades. In particular the stability

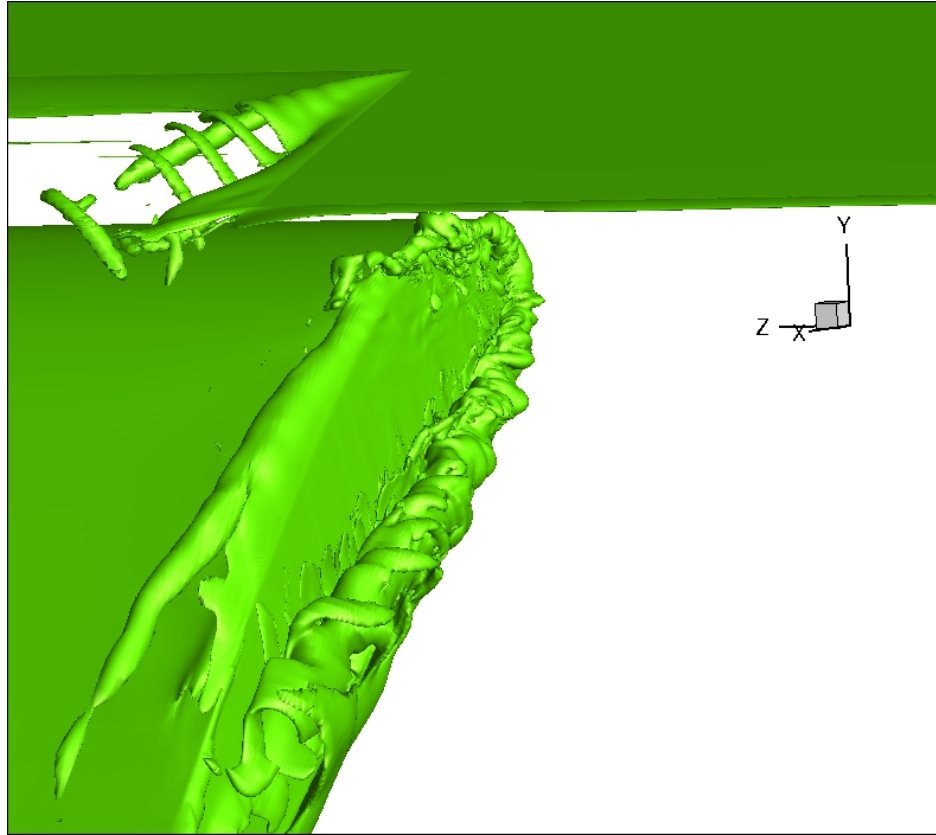


Figure 8. Isosurface of instantaneous vorticity magnitude,  $|\omega| = 500 U_\infty/c$  from the DES.

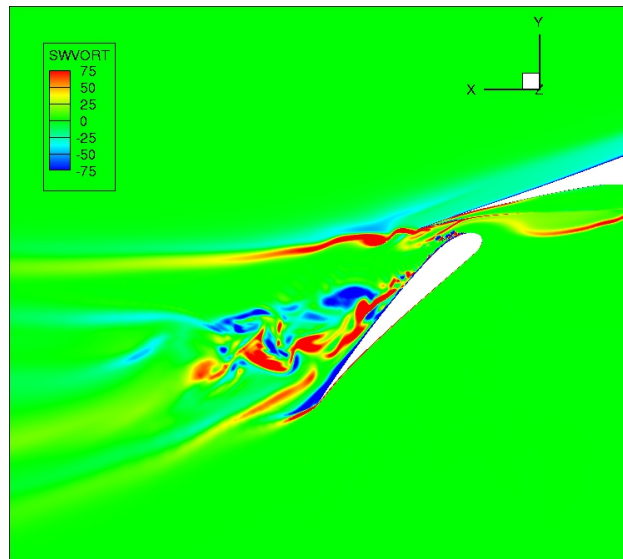


Figure 9. Contour map of instantaneous spanwise vorticity  $\omega_z U_\infty/c$  on the midspan plane from the DES.

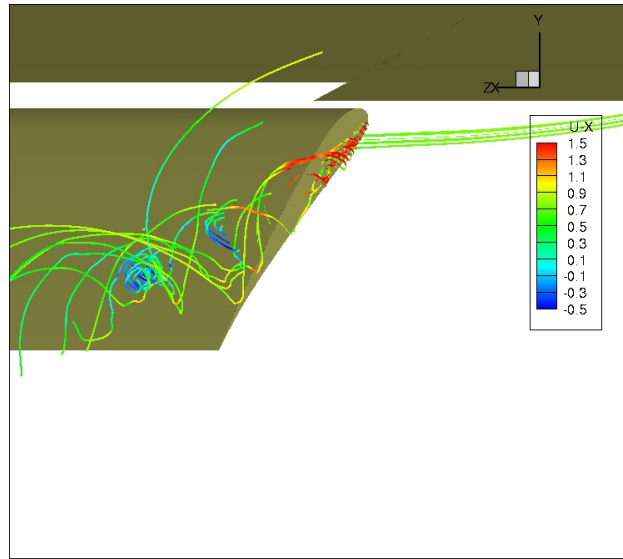
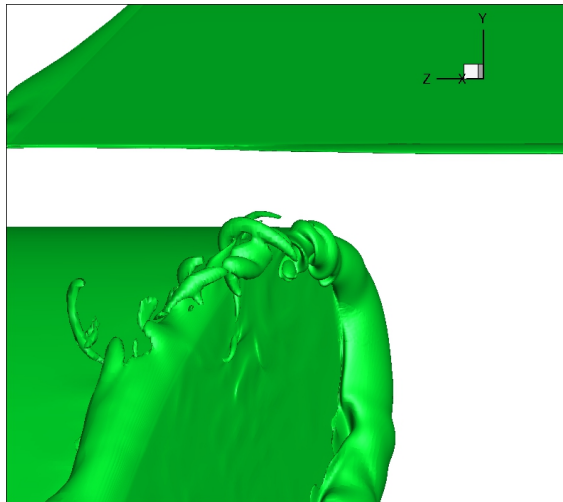
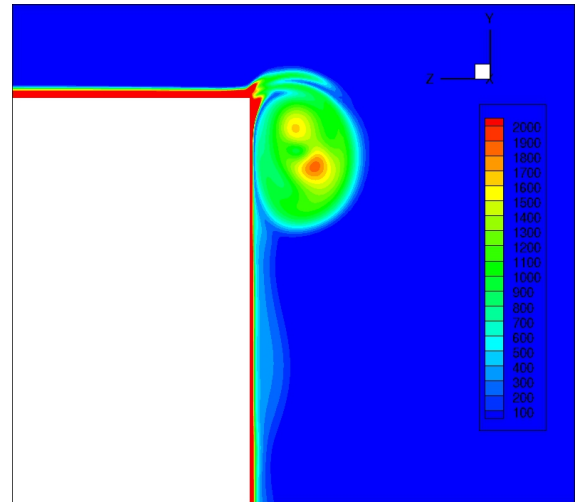


Figure 10. Instantaneous velocity streamlines coloured by the streamwise velocity component normalized by  $U_\infty$  from the DES highlighting the vortex breakdown occurring above the flap trailing edge.



(a) Isosurface of vorticity magnitude  $|\omega| = 1000 U_\infty / c$



(b) Contour map of vorticity magnitude  $|\omega|c/U_\infty$  on a slice through the primary vortex

Figure 11. Helical structure of instability leading to breakdown from the large filter DES.

characteristics of the Batchelor  $q$ -vortex, initially proposed as a model for an aircraft trailing vortex,<sup>15</sup> have been extensively mapped out for a wide range of swirl levels (specified by  $q$ ), background flow and Reynolds numbers. Lessen et al.<sup>24</sup> discovered a set of inviscid instability modes occurring in vortices with non-zero swirl less than a critical value of  $q \approx 1.5$ . The unstable modes had a non-axisymmetric, helical structure with azimuthal wavenumbers  $m \leq 1$  for a vortex with a jet-like axial velocity profile. The maximum growth rate at each negative azimuthal wavenumber increased with  $|m|$ . The peak value of the growth rates occurred at  $q \approx 0.87$ . Viscosity was found to have a stabilising effect on the inviscid modes.<sup>25,26</sup> As a result the unstable modes at each Reynolds number are confined to a finite range of azimuthal wavenumbers. Heaton<sup>27</sup> showed that inviscid instability modes also existed in the range  $1.5 \leq q \leq 2.31$  but with far lower maximum growth rates. Apart from the inviscid modes, purely viscous instability modes were also discovered<sup>26,28</sup> with growth rates orders of magnitude smaller than the inviscid modes.

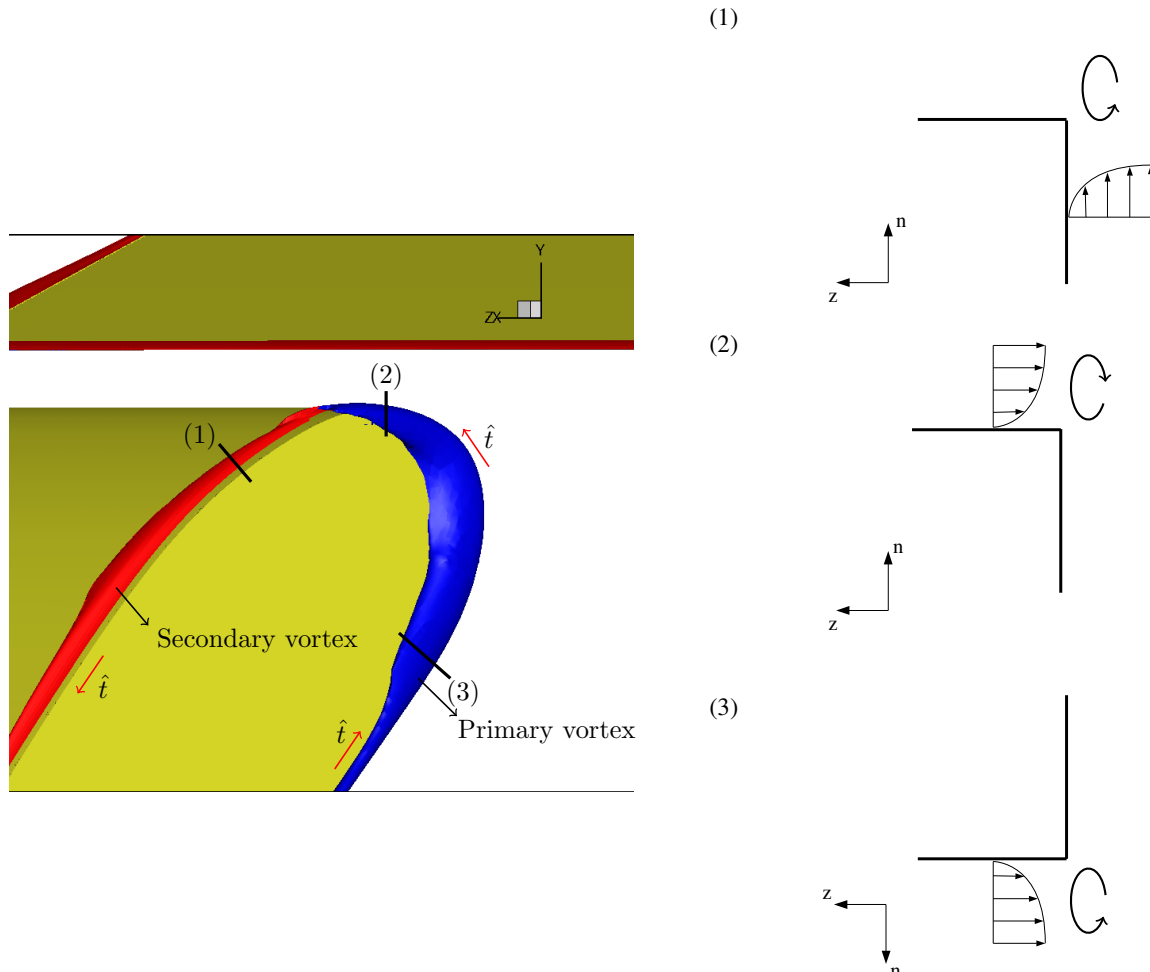


Figure 12. Left: Isosurface of vorticity magnitude from steady RANS solution colored by the sign of the vorticity component along the local side-edge tangent, positive by red and negative by blue. Right: Schematic of flow separation and roll-up at different locations along the side-edge. The sections are normal to the side-edge tangent vector  $\hat{t}$ .

The jet-like or wake-like character of the axial velocity profile of the columnar vortex affects the temporal stability in the following manner. If a vortex with a swirl strength of  $q$  and a jet-like axial velocity profile has an unstable mode with an azimuthal wavenumber  $m$ , then a vortex with the same strength and a wake-like axial velocity profile has an unstable mode with the same axial wavenumber and a azimuthal wavenumber of  $-m$  with the same growth rate.

In the present flow, in the region where the primary vortex begins (section 2 in figure 12) the vortex axis is directed along the local  $-\hat{t}$  direction. The axial velocity component along this direction is negative on the

centerline and decreases with distance from the vortex axis. Therefore it has a jet-like axial velocity profile. For a columnar vortex with a jet-like axial velocity profile, the azimuthal wavenumbers of the unstable inviscid modes are negative (apart from  $m = 1$ ) which implies that the winding of the helical waves is along the same direction as the rotation of the vortex. As seen in figure 11 the sense of winding of the helical instability in this region is consistent with this behaviour and also along the vortex axis direction. The vortex profile is not axisymmetric and is confined by the presence of the wall. However it is useful to find the approximate value of  $q$  for an equivalent Batchelor vortex. Using the DES mean flow, the core profiles of the primary vortex in this region were examined. Based on average values around the azimuth, a typical value of  $q \approx 1.0$  was obtained which is within the swirl level range required for inviscid instability. This suggests that the inviscid instability occurring in columnar vortices with axial flow is a likely candidate for the leading edge instability in the present case. A detailed stability analysis of the base flow using an appropriate model for the side-edge vorticity field is required to ascertain the nature of the instability.

### *V.B.2. Unsteady surface pressure field*

The leading edge instability is a potential key noise source due to its location near the side-edge which can efficiently scatter the noise to the far-field. The samples of the instantaneous DES flowfield were analysed to obtain the temporal Fourier components of the unsteady surface pressure on the flap surface. The sampling rate of  $0.0015 c/U_\infty$  corresponds to a Nyquist frequency of  $\approx 333.33 U_\infty/c$ . Contour maps on the side face of the flap and the upper suction surface of the Fourier modes at frequencies of  $32 U_\infty/c$ ,  $52 U_\infty/c$ ,  $82 U_\infty/c$  and  $132 U_\infty/c$  are presented in figures 13 and 14 respectively. In the NASA Langley aeroacoustic experiment, these correspond approximately to frequencies of 4.8 kHz, 7.8 kHz, 12.3 kHz and 19.8 kHz.

The pressure fluctuations on the flap side are present along the reattachment region of the primary vortex and correspond to the helical instability of the primary vortex. The high frequency Fourier modes are confined to the region close to the leading edge. Whereas the lower frequency modes are spread over the entire path of the primary vortex. On the suction surface, the fluctuations are largely constituted by the low frequency modes and the downstream extent of the modes increases with decreasing frequency. The peak on the side-edge corresponds to the location at which the primary vortex crosses the side-edge. The fluctuations on the suction surface correspond to the interaction of the vortex with the surface after it crosses over. These results are consistent with the acoustic measurements from both NASA Ames and NASA Langley which showed that the centroid of the noise source distribution moved downstream with decreasing frequency. It should be noted that the relevant quantity on the airfoil surfaces required for obtaining the noise field is the acoustic pressure of which the pressure field from the present DES comprises only the hydrodynamic part.

## **VI. Summary and future work**

The Spalart-Allmaras based RANS obtained the key features of the mean flowfield and matched the previous experimental and RANS studies closely. The mean flowfield from the detached eddy simulation was shown to provide a more accurate picture of the time-averaged flap side-edge flowfield. The DES also captured the unsteady features of the flow including the turbulent side-edge vorticity field, the unsteady merged vortex and the vortex breakdown above the flap trailing edge. An instability of the primary vortex near the leading edge was found to lead to the breakdown to turbulence. The inviscid instability mode occurring in vortices with axial flow was identified as a likely candidate for the instability of the primary vortex.

In future work the unsteady, incompressible flowfield solution from the present DES, in particular the information about the aeroacoustic noise sources, will be used to compute the acoustic pressure in the farfield using an acoustics module<sup>29</sup> which solves the Lighthill equation using a boundary element method. The relative contributions of the different unsteady features of the flap side-edge flowfield will be ascertained.

## **Acknowledgments**

This research is supported by NASA's Transformational Tools and Technologies and Advanced Air Transport Technologies projects through an appointment to the NASA Postdoctoral Program at Ames Research Center. The appointment is administered by Oak Ridge Associated Universities through a contract with NASA. We would like to thank Dr. Mehdi Khorrami, Dr. James Ross and Dr. Solkeun Jee for their valuable

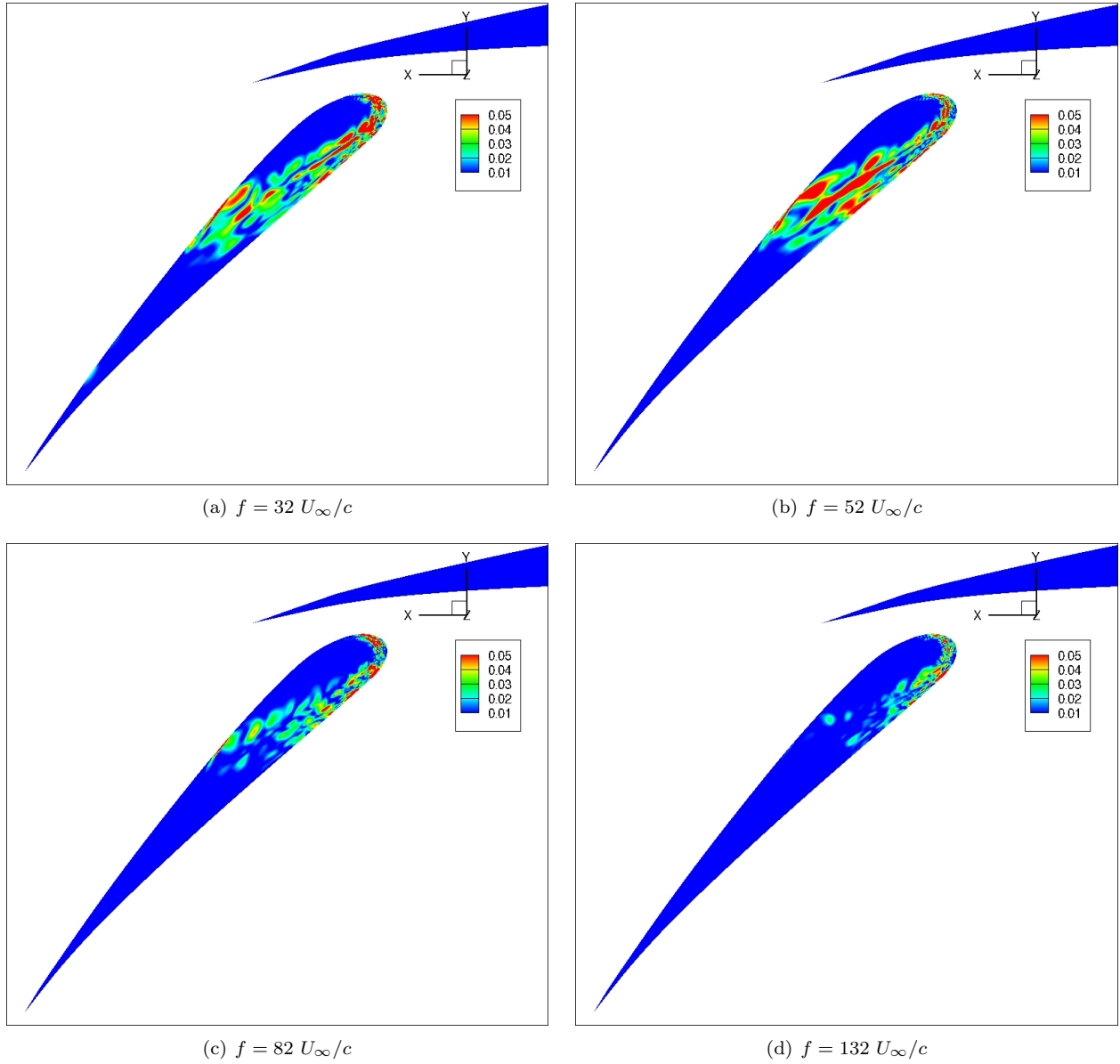


Figure 13. Contour map of the normalized values of the Fourier modes of unsteady pressure field,  $\hat{P}(f)/U_\infty^2$ , at different frequencies on the flap side face.

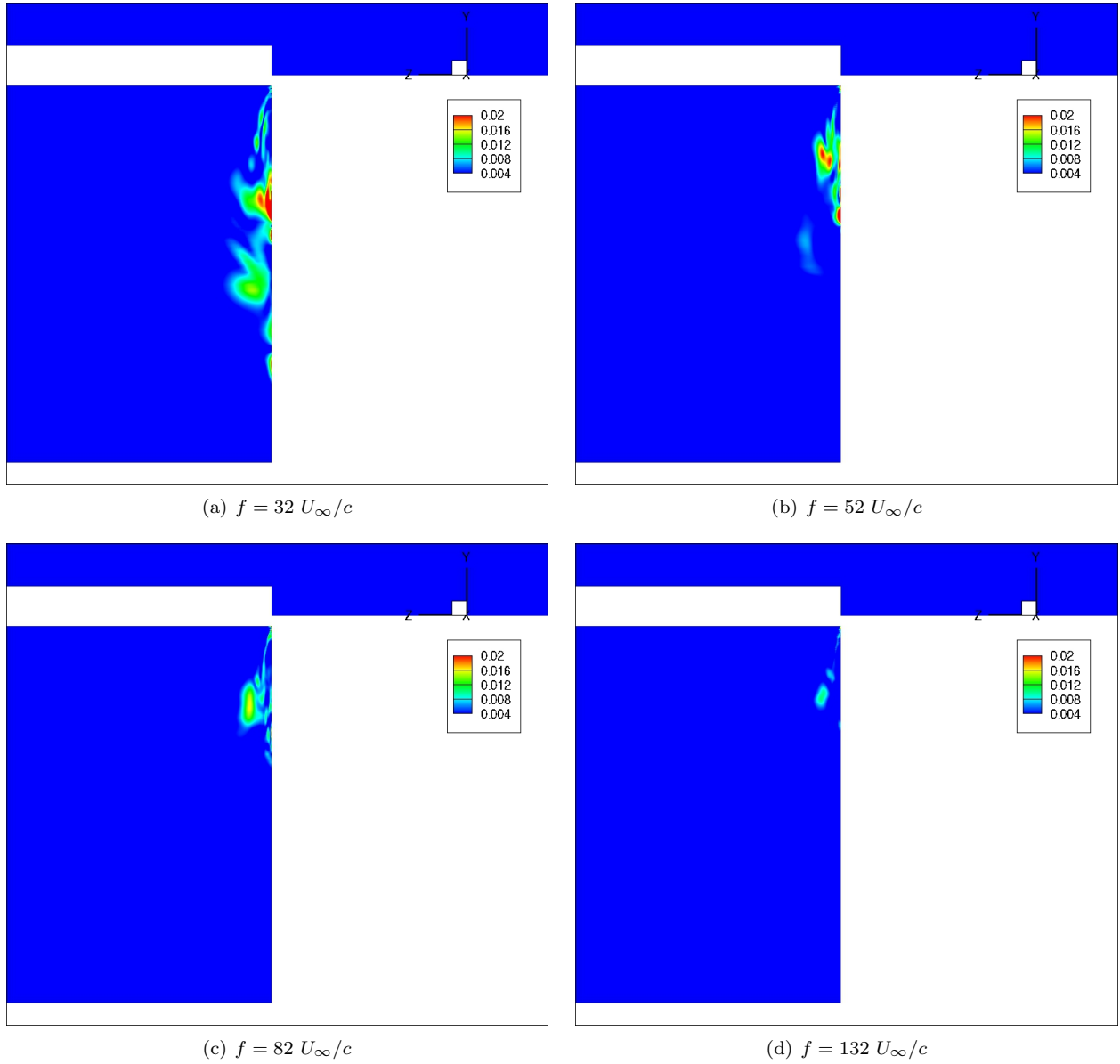


Figure 14. Contour map of the normalized values of the Fourier modes of unsteady pressure field,  $\hat{P}(f)/U_\infty^2$ , at different frequencies on the upper suction surface of the flap. The view is from a downstream location along the  $-x$  direction.



advice and support.

## References

- <sup>1</sup>Storms, B. L., Takahashi, T. T., and Ross, J. C., "Aerodynamic influence of a finite-span flap on a simple wing," SAE paper 951977, Sept. 1995.
- <sup>2</sup>Radeztsky, R. H., Singer, B. A., and Khorrami, M. R., "Detailed measurements of a flap side-edge flow field," AIAA paper 98-0700, 1998.
- <sup>3</sup>Khorrami, M. R., Singer, B. A., and Radeztsky, R. H., "Reynolds-averaged Navier-Stokes computations of a flap side-edge flow field," *AIAA Journal*, Vol. 37, No. 1, 1999, pp. 14-22.
- <sup>4</sup>Takallu, M. A. and Laffin, K. R., "Reynolds-averaged Navier-Stokes simulations of two partial-span flap wing experiments," AIAA paper 98-0701, 1998.
- <sup>5</sup>Meadows, K. R., Brooks, T. F., Humphreys, W. M., Hunter, W. W., and Gerhold, C. H., "Aeroacoustic measurements of a wing-flap configuration," AIAA paper 97-1595, 1997.
- <sup>6</sup>Brooks, T. F. and Humphreys, W. M., "Flap-edge aeroacoustic measurements and predictions," *Journal of Sound and Vibration*, Vol. 261, No. 1, 2003, pp. 31-74.
- <sup>7</sup>Lilley, G. M., "The prediction of airframe noise and comparison with experiment," *Journal of Sound and Vibration*, Vol. 239, No. 4, 2001, pp. 849-859.
- <sup>8</sup>Kendall, J. M. and Ahyte, W. F., "Noise generation by a lifting wing/flap combination at Reynolds numbers to  $2.8 \times 10^6$ ," AIAA paper 80-0035, 1980.
- <sup>9</sup>Hayes, J. A., Horne, W. C., Soderman, P. T., and Bent, P. H., "Airframe noise characteristics of a 4.7% scale DC-10 model," AIAA paper 97-1594, 1997.
- <sup>10</sup>Hardin, J. C., "Noise radiation from the side edges of flaps," *AIAA Journal*, Vol. 18, No. 5, 1980, pp. 549-552.
- <sup>11</sup>Meecham, W. C., "Aerosound from corner flow and flap flow," *AIAA Journal*, Vol. 21, No. 2, 1983, pp. 228-234.
- <sup>12</sup>Howe, M. S., "On the generation of side-edge flap noise," *Journal of Sound and Vibration*, Vol. 80, No. 4, 1982, pp. 555-573.
- <sup>13</sup>Sen, R., "Vortex-Oscillation model of airfoil side-edge noise," *AIAA Journal*, Vol. 35, No. 3, 1997, pp. 441-449.
- <sup>14</sup>Khorrami, M. R. and Singer, B. A., "Stability analysis for noise-source modeling of a part-span flap," *AIAA Journal*, Vol. 37, No. 10, 1999, pp. 1206-1212.
- <sup>15</sup>Batchelor, G. K., "Axial flow in the trailing line vortices," *Journal of Fluid Mechanics*, Vol. 20, 1964, pp. 645-658.
- <sup>16</sup>Michalke, A. and Timme, A., "On the inviscid instability of certain two-dimensional vortex-type flows," *Journal of Fluid Mechanics*, Vol. 29, 1967, pp. 647-666.
- <sup>17</sup>Imamura, T., Enomoto, S., Kato, H., Yokokawa, Y., and Yamamoto, K., "Numerical simulation of NACA0012 wingtip flow leading to noise generation," 11th AIAA/CEAS aeroacoustics conference (26th AIAA aeroacoustics conference), 2005.
- <sup>18</sup>Street, C. L., "Numerical simulation of fluctuations leading to noise in a flap-edge flowfield," AIAA paper 98-0628, 1998.
- <sup>19</sup>Langtry, R. B., Gren, E. A., Larssen, J. V., and Spalart, P. R., "Evaluation of structured and unstructured grids for detached eddy simulation of flap edge noise," 15th AIAA/CEAS aeroacoustics conference (30th AIAA aeroacoustics conference), 2009.
- <sup>20</sup>Ham, F. and Iaccarino, G., "Energy conservation in collocated discretization schemes on unstructured meshes," Center of turbulence research annual research briefs, 2004.
- <sup>21</sup>Mahesh, K., Constantinescu, G., and Moin, P., "A numerical method for large-eddy simulation in complex geometries," *Journal of Computational Physics*, Vol. 197, No. 1, 2004, pp. 215-240.
- <sup>22</sup>Spalart, P. R., Deck, S., Shur, M. L., Shires, K. D., Strelets, M., and Travin, A., "A new version of detached-eddy simulation, resistant to ambiguous grid densities," *Theoretical and Computational Fluid Dynamics*, Vol. 20, No. 3, 2006, pp. 181-195.
- <sup>23</sup>Shur, M., Spalart, P. R., Strelets, M., and Travin, A., "Detached-eddy simulation of an airfoil at high angle of attack," *Engineering turbulence modelling and experiments*, Vol. 4, 1999, pp. 669-678.
- <sup>24</sup>Lessen, M., Singh, P. J., and Paillet, F., "The stability of a trailing line vortex. Part 1. Inviscid theory," *Journal of Fluid Mechanics*, Vol. 63, 1974, pp. 753-763.
- <sup>25</sup>Lessen, M. and Paillet, F., "The stability of a trailing line vortex. Part 1. Viscous theory," *Journal of Fluid Mechanics*, Vol. 65, 1974, pp. 769-779.
- <sup>26</sup>Khorrami, M. R., "On the viscous modes of instability of a trailing line vortex," *Journal of Fluid Mechanics*, Vol. 225, 1991, pp. 197-212.
- <sup>27</sup>Heaton, C. J., "Centre modes in inviscid swirling flows and their application to the stability of the Batchelor vortex," *Journal of Fluid Mechanics*, Vol. 576, 2007, pp. 325-348.
- <sup>28</sup>Fabre, D. and Jacquin, L., "Viscous instabilities in trailing vortices at large swirl numbers," *Journal of Fluid Mechanics*, Vol. 500, 2004, pp. 239-262.
- <sup>29</sup>Khalighi, Y., Mani, A., Ham, F., and Moin, P., "Prediction of Sound Generated by Complex Flows at Low Mach numbers," *AIAA Journal*, Vol. 48, No. 2, 2010.